**Annales
Geophysicae**

A very bright SAR arc: implications for extreme magnetosphere-ionosphere coupling

J. Baumgardner[1], J. Wroten[1], J. Semeter[1], J. Kozyra[2], M. Buonsanto[3], P. Erickson[3], and M. Mendillo[1]

[1]Center for Space Physics, Boston University, Boston, MA, USA
[2]Department of Atmospheric, Oceanic and Space Science, University of Michigan, Ann Arbor, MI, USA
[3]MIT Haystack Observatory, Westford, MA, USA

Abstract. In contrast to the polar aurora visible during geomagnetic storms, stable auroral red (SAR) arcs offer a subvisual manifestation of direct magnetosphere-ionosphere (M-I) coupling at midlatitudes. The SAR arc emission at 6300 Å is driven by field-aligned magnetospheric energy transport from ring current/plasmapause locations into the ionosphere-thermosphere system. The first SAR arc was observed at the dawn of the space age (1956), and the typical brightness levels and occurrence patterns obtained from subsequent decades of observations appear to be consistent with the downward heat conduction theory, i.e., heated ambient F-layer electrons excite oxygen atoms to produce a spectrally pure emission. On very rare occasions, a SAR arc has been reported to be at brightness levels visible to the naked eye. Here we report on the first case of a very bright SAR arc ($\sim$13 kilo-Rayleighs) observed by four diagnostic systems that sampled various aspects of the sub-auroral domain near Millstone Hill, MA, on the night of 29 October 1991: an imaging spectrograph, an all-sky camera, an incoherent scatter radar (ISR), and a DMSP satellite. Simulations of emission using the ISR and DMSP data with the MSIS neutral atmosphere succeed in reproducing the brightness levels observed. This provides a robust confirmation of M-I coupling theory in its most extreme aeronomic form within the innermost magnetosphere ($L\sim$2) during a rare superstorm event. The unusually high brightness value appears to be due to the rare occurrence of the heating of dense ionospheric plasma just equatorward of the trough/plasmapause location, in contrast to the more typical heating of the less dense F-layer within the trough.

Keywords. Ionosphere (Ionosphere disturbance) – Magnetospheric physics (Magnetosphere-ionosphere interactions) – Atmospheric composition and structure (Airglow and aurora)

Correspondence to: M. Mendillo
(mendillo@bu.edu)

1 Introduction

Extreme events in the solar-terrestrial system offer rare opportunities to test the limits of geophysical mechanisms that operate at more moderate levels under nominal solar and geomagnetic conditions. These extreme events may also produce emergent phenomena not seen during more moderate events. The exact features that define a *superstorm* are still under investigation, and thus superstorms are defined in relative terms as the strongest 2% of magnetic storm events (Bell et al., 1997) or in absolute terms as magnetic storms below a threshold of $Dst=-240$ nT. Case studies of superstorms bring to the field of solar-terrestrial physics a set of challenges broader in scope and potentially more significant in impact than come from the statistical treatment of many storm-time disturbances. In this paper, we address a specific magnetosphere-ionosphere coupling process, the instigation of stable auroral red (SAR) arcs. The issues involved are (a) the generation of 6300 Å emission from atomic oxygen excited to the O(^{1}D) state via impact by hot ionospheric electrons (e*), (b) the mechanism(s) that heated the ambient electrons (e$^-$), and (c) the strength of magnetospheric convection that regulates how far the sub-auroral domain extends towards the equator.

The study of SAR arcs has benefited from a series of fundamental papers and review articles. Just five years after the publication of the discovery of SAR arcs by Barbier (1958), Roach and Roach (1963) presented a strikingly complete status report on observations and proposed theories. Shortly thereafter, Cole (1965) gave the now accepted explanation of heating by thermal conduction from the ring current. The review paper by Hoch (1973) then summarized, in a clear and insightful fashion, the status of a field barely 15 years old, linking optical observations to plasmapause/ring current characteristics in the inner magnetosphere. The final major contribution of the first two decades of SAR arc research came from Rees and Roble (1975), providing an overall
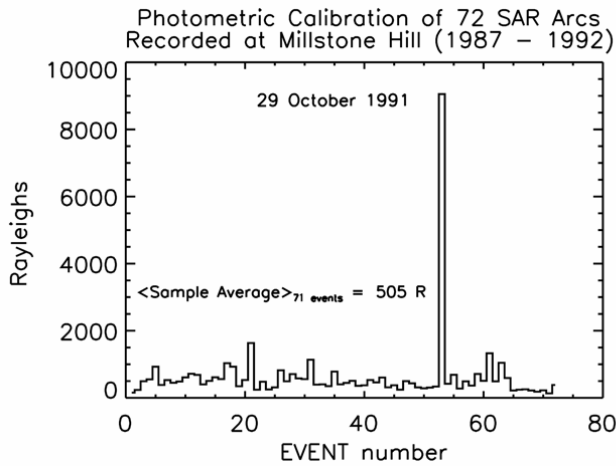
Fig. 1. Characterization of 72 SAR arc events by observed brightness in Rayleighs (R) above background. No atmospheric extinction corrections have been made.
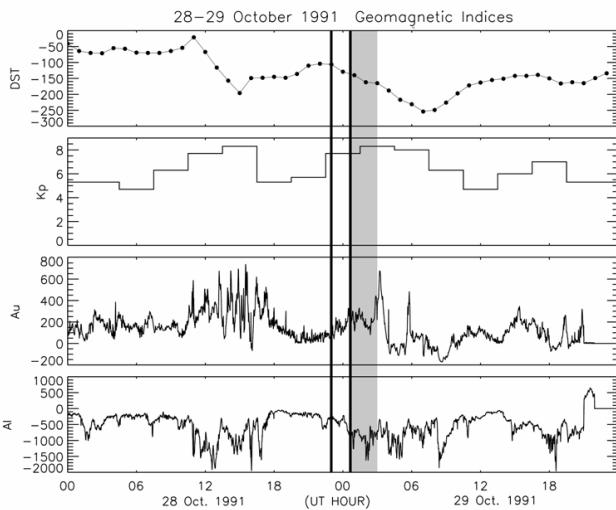

Fig. 2. Geomagnetic indices Dst, Kp, AU and AL for the storm period 28–29 October 1991. The period of optical observations at Millstone Hill is shown by the shaded time period, and the times of two DMSP passes are indicated by the solid vertical lines.

summary of observational characteristics and occurrence patterns and, most importantly, they offered a comprehensive formalism for calculating SAR arc emission. Two solar cycles later, Kozyra et al. (1997) re-energized the topic of SAR research by describing the physics of magnetosphere-ionosphere (M-I) coupling that links the ring current energy budget to the ionosphere-thermosphere along the plasmapause/trough geomagnetic field lines. The reader is referred to those important summaries, and their detailed set of references, for more information on SAR arcs.

Why should a case-study of a single SAR arc be needed now? The event observed on the night of 29 October 1991

may well be the brightest one in the "modern era" (i.e., post 1975) and, in the 50th anniversary year of SAR arc discovery, our diagnostic capabilities are sufficiently advanced to use this event to constrain processes and mechanisms to degrees not possible before.

To show the observational rarity of this event, Fig. 1 gives a summary of 72 brightness-calibrated SAR arcs observed at Millstone Hill during the period 1987–1992 when the same detector was used thereby assuring consistency in calibration. The average brightness of 71 events was ~500 Rayleighs (R) with the SAR arc of 29 October 1991 a very major outlier in the distribution. For geophysical context, Fig. 2 presents a summary of geomagnetic indices that place this event within the realm of a super-storm.

SAR arcs are almost always sub-visual features, and thus optical diagnostics are limited to dark sky conditions. The hours of central interest to this study are therefore indicated by shading in Fig. 2. In addition to the Boston University optical instruments at Millstone Hill, there is, of course, the on-site incoherent scatter radar (ISR) that provides supporting observations of the local ionosphere. Complementing both on this night were space-based in-situ data available from over-flights of two Defense Meteorological Satellite Program (DMSP) vehicles that provide important multi-diagnostic coverage of plasma parameters inaccessible to the ISR on this night. The times of the DMSP passes are indicated by the dark vertical lines in Fig. 2.

2 Observations

2.1 Observational systems

Two state-of-the-art optical imaging instruments were in operation at Millstone Hill in October 1991: an all-sky, low-light-level imaging system and a wide-angle meridional imaging spectrograph. The design and operational characteristics of both systems are described fully in Baumgardner et al. (1993). Briefly, the all-sky camera takes images at multiple wavelengths via the sequential use of narrow band filters (~12 Å FWHP). Of relevance to this study are the data taken using the filters at 6300 Å, the classic 'red-line' emission from thermospheric oxygen, and control/background images taken at 6444 Å, used to assess the continuum near 6300 Å and atmospheric conditions (clouds, etc). The output of an all-sky camera is thus brightness versus 2-dimensional space, at on- and off-band wavelengths, throughout the night. Spatial structures so captured provide independent science yield from the emission observed, as well as the broad context to help in the interpretation of traditional line-of-sight diagnostic systems (e.g., radar beams and satellite passes).

The imaging spectrograph employed a slit ~180° long by ~1° wide projected upon the sky along the meridian. A 600 lines/mm plane grating dispersed the light resulting in wavelength coverage from 5400 Å to 7400 Å, and thus the
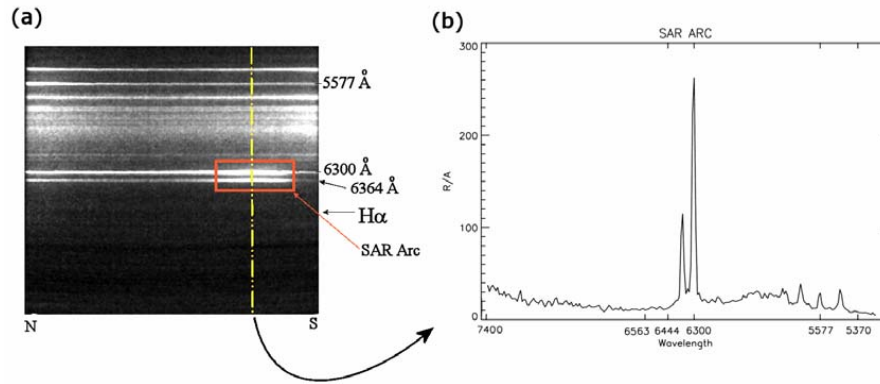
Fig. 3. (a) A sample image from the meridional imaging spectrograph. The spatial location of the SAR arc is indicated by the red box, which encloses a pronounced bright "bulge" absent from other emission lines. The vertical yellow line refers to a 1-pixel width column taken at the brightest area of the SAR arc, plotted as a spectrum (R/Å vs. wavelength) in **(b)**.

data product is meridional brightness versus latitude (N-S), at many wavelengths simultaneously, throughout the night. A sample spectrum is shown in Fig. 3, one that demonstrates the spectral purity of the SAR arc redline emission in comparison to other terrestrial emission lines. The absence of auroral signatures in 5577 Å is in marked contrast to the ~200 kR redline emission accompanied by ~100 kR of greenline above Millstone Hill during the great aurora of 23–24 March 1969 (Noxon and Evans, 1976).

The capabilities of the Millstone Hill ISR have been described in many papers (e.g., Evans and Loewenthal, 1964; Foster et al., 1994). The parameters of relevance to SAR arc studies are height profiles of the electron density (N_e), electron temperature (T_e) and ion temperature (T_i). Use of the Millstone Hill ISR in support of SAR arcs began on the very first night of imager operations at Millstone Hill (Mendillo et al., 1987), and later in case-study work by Foster et al. (1994).

The DMSP satellite has also been described in many previous studies (e.g., Greenspan et al., 1986; Rich and Hairston, 1994), and recently in a concise way by Mishin et al. (2004). Of relevance to SAR arcs are the observed values of total ion density (assumed equal to N_e), together with T_e and T_i, all at the satellite height of ~840 km. Prior use of DMSP data in conjunction with ISR observations for SAR arc studies appears in Foster et al. (1994), and for the trough in Mishin et al. (2004).

2.2 Datasets

Figure 4 presents a sample of the all-sky images at 6300 Å observed from Millstone Hill on the night of 29 October 1991. Figure 5 gives an independent measure of the time history of redline emission vs. latitude as observed by the imaging spectrograph. In both cases, there is a clear separation of the equatorward edge of the diffuse aurora (to the north in each data set) from the SAR arc that passed through zenith to latitudes well equatorward of Millstone Hill. To justify the remarkable levels of brightness in Rayleighs (R) shown by the color bars in both figures, we need to address methods of calibration.

2.3 Calibration

(a) All-sky imager

The reduction of all sky images is not a trivial matter. There are complex issues to address involving background emissions, atmospheric scattering, instrument scattering and challenges associated with the proper flat fielding of a fish-eye lens system. A formal description of calibration methods is given in the Appendix (from Semeter, 1997), and thus only a brief summary is given here. We begin the process by dark subtracting and normalizing the images to a single exposure time. In order to compensate for instrumental scattering and light leaks, we use an opaque disk in place of a filter and take open-shutter darks. We create a flat-field image by first placing an opal glass disc at the filter location then showing the system a light source. The opal glass acts as a diffuser, resulting in a uniform source of illumination from the filter plane to the detector. This compensates for varying sensitivities on the CCD chip and camera lens, but does not address the varying throughput associated with the all sky lens system, namely lens vignetting. This is handled by exposing the system to our calibration light source at regular overlapping angles along a meridian of our glass dome. We then fit a curve to those data and construct a 2-D image which we use to divide out the all sky lens vignetting.

Absolute calibration begins with our standard light source, a 3-inch phosphor disk activated by ^{14}C. This emits a range of known brightnesses in RÅ^{-1} extending from 5000 Å to 7800 Å, with 104 RÅ^{-1} at 6300 Å and 94 RÅ^{-1} at 6444 Å, the wavelengths of interest for this data set. The system is shown this light source at the zenith point, through both
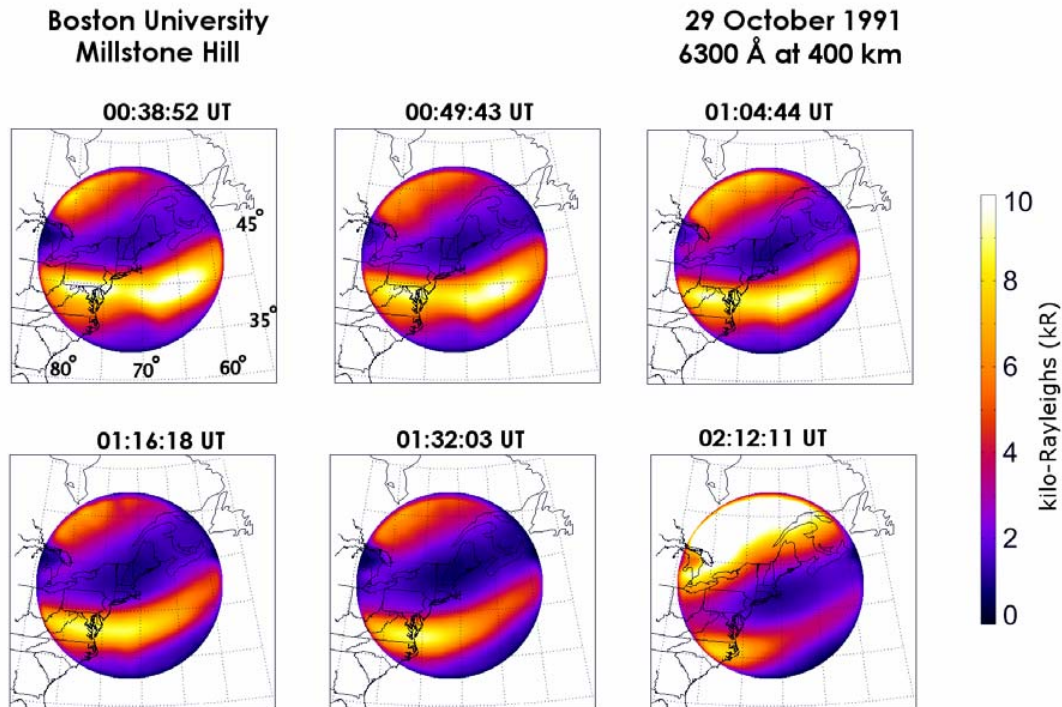
Fig. 4. A sample of the all-sky images at 6300 Å taken at Millstone Hill on the night of 29 October 1991. Observations above 15° elevation angle are mapped upon a geographic grid ("unwarped" from the fish-eye lens view) providing a 150° field of view (FOV) using an emission height of 400 km appropriate for the SAR arc. Brightness units are in Rayleighs (R). The emissions to the north of the SAR arc are the diffuse aurora that occur near altitudes of ∼200 km.
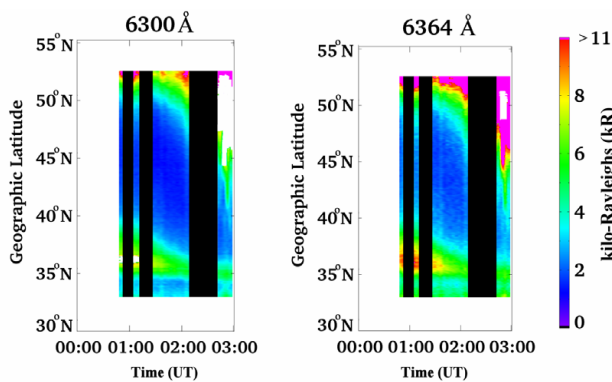

Fig. 5. Meridional imaging spectrograph data taken at Millstone Hill on the night of 29 October 1991. Shown are the brightness levels versus latitude (assuming a 400 km emission height for 6300 Å and 6364 Å) over a 150° FOV as a function of time. Brightness levels are given in Rayleighs (R). No significant levels of emission were observed in the vicinity of the SAR arc at any other wavelength observed over the range 5400 to 7400 Å. Data gaps were due to either detector saturation (white) or periods when the observers were adjusting exposure times (black). The 6364 Å brightness was scaled to the 6300 Å brightness (see text).

onband (6300 Å) and offband filters (6444 Å) at a series of different exposure times. These calibration images are dark-subtracted, flat fielded and all issues of filter bandwidth, filter transmission and exposure times are accounted for. The reduced data images are then compared with these calibration images. Background emissions were assessed by averaging a series of 6444 Å images taken on the same night of the event (00:30 UT∼02:30 UT). These offband images are scaled to account for differences in the filter transmission curves and continuum levels at 6300 Å and 6444 Å. Finally, there are no corrections made for the possible atmospheric scattering and extinction of the signals coming from the either the SAR arc or the diffuse aurora. There were no stars visible in any of the images due to the strong auroral and sub-auroral emissions and the short exposure times (0.5 s) used.

(b) Meridional imaging spectrograph

A different set of concerns and methods are required for spectra reduction. We again expose our system to the ^{14}C source at several overlapping angles along the meridian. In the case of a spectrograph, this series of images will simultaneously address issues of absolute calibration (source of known brightness), flat fielding (source of uniform constant brightness) and lens vignetting (multiple angles along the

meridian), due to the 1-D nature of a spectrograph's FOV. All images are dark subtracted and exposure times are normalized. Spectral line curvature is addressed by fitting a 2nd order polynomial along the emission line. Spectral dispersion is determined by fitting a 3rd order polynomial to several identified emission lines along the spectral image. We extract the light along the 6300 Å emission line, using an 11-pixel width in order to accommodate the SAR arc light, then multiply by the 9.25 Å/pixel dispersion to get the total flux of the line. Continuum background emission is removed by subtracting a width equal to that used for the emission line (in this case, 11-pixels) at a location with no emission line. 6300 Å airglow is removed by subtracting the average zenith brightness at the 6300 Å line (use of zenith for control data is appropriate because the SAR arc was always south of zenith while the diffuse aurora was always north of zenith during the time period of interest).

As can be seen from the left panel in Fig. 5, there were periods when the spectrograph had saturated signals in the brightest part of the SAR arc (near 01:00 UT) and in the diffuse aurora (near 03:00 UT). Fortunately, there are three emissions generated by the O(^{1}D) state, namely at 6300 Å, 6364 Å and 6392 Å. The Einstein coefficients for these transitions are .0059/s, .0018/s, and 1.1×10^{-6}/s, respectively (Semeter et al., 1996). We thus could use the 6364 Å data from the spectrograph which was fainter and unsaturated and scale it to the 6300 Å emission levels using the known ratio of Einstein coefficients for these two transmissions:

$$B_{\text{SAR}}(6300\text{Å}) = (A_{6300}/A_{6364}) \times B_{\text{SAR}}(6364\text{Å})$$

which for the values above yields a ratio that is 3.27.

The results of this cross comparison using two instruments are shown in Fig. 6.

The peak 6300 Å brightness value for the event is ~10.8 kR, which reduces to ~9.5 kR above sky-background, a value that approaches naked-eye visibility. If a simple "extinction correction" is appropriate for the conditions on this night, a multiplicative factor of ~1.4 for a zenith angle of 45° would be used (Allen, 1973). This brings the SAR arc to 13.4 kR, for its above-the-atmosphere value. Our search of the literature did not result in any prior 2-D image of a SAR arc brighter than this one.

3 Modeling

3.1 Formalism and input requirements

In their classic description of SAR arc generation, Rees and Roble (1975) described how heated ionospheric electrons (e* at T_e) collide with atomic oxygen (O) to excite it to the ^{1}D state, with subsequent emission of photons at 6300, 6364 and 6392 Å. By computing the production and loss of O(^{1}D), and equating them under the assumption of photochemical
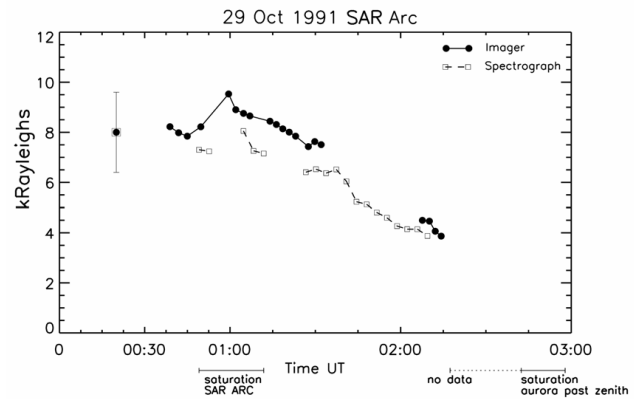

Fig. 6. Independent calibration results for the all-sky imager and the meridional imaging spectrograph operating at Millstone Hill on the night of 29 October 1991. The curves give the total above sky-background brightness values vs UT from each instrument: for the spectrograph this is the brightest value of the SAR arc along the north-south meridian; for the imager it is the brightness value at the corresponding spatial location and time. The uncertainty levels for each system ultimately depend on the ^{14}C standard source that has a ~20% variation within its disk, and so a 20% "uncertainty" bar is indicated.

equilibrium, the emission brightness (in Rayleighs) can be obtained.

The production function may be portrayed as an energy excitation reaction for oxygen atoms

$$\text{e*} + \text{O} \xrightarrow{k} \text{e} + \text{O*}(^1\text{D}) \tag{1}$$

where k is the effective reaction rate for energy transfer.

Since 1.96 eV is added to the O atoms with each reaction, Rees and Roble (1975) treated it as a heat transfer problem from the electron gas to the oxygen gas, with an energy excitation rate as

$$E(\text{O}^1\text{D}) = k[\text{e*}][\text{O}](\text{units of eV/cm}^3/\text{s}) \tag{2}$$

where brackets denote concentrations in #/cm^3. An analytic approximation for the RHS of (2), effectively computing k from the cooling rate of the electrons, had been derived earlier by Rees et al. (1967) and it appears as Eq. (61) in Rees and Roble (1975), expressed as a parameterization using electron temperature. Converting from a production rate for heat to one for concentration can be done simply as

$$P(\text{O*}) = E(\text{O}^1\text{D})/1.96(\text{units now } \#\text{O*}/\text{cm}^3/\text{s}) \tag{3}$$

This [O*(^{1}D)] production rate then can be computed using values of the electron and oxygen concentrations and electron temperature via Eq. (61) in Rees and Roble (1975).

The loss rate of O* comes from two sources:

(a) Collisional de-excitation ("quenching"):

$$L_{\text{quench}} = \Sigma_k q_k[X]_k[\text{O*}] = Q_T[\text{O*}] \tag{4}$$

where X are the individual species colliding with O* (e.g., N_2, O_2, O, e^-) and q_k are their respective quenching reaction rates (see Table 1 in Semeter et al., 1996). The summation yields the total quenching rate Q_T.

(b) Photon emission:

Expressed as a spontaneous emission reaction,

$$O^* \xrightarrow{A_{1D}} O + \text{photon} \tag{5}$$

where A_{1D} is the Einstein rate coefficient for all possible radiation pathways out of the ^{1}D state. This loss process by emission may be cast as a volume emission rate

$$L_{\text{emission}} = d[\text{photons/cm}^3]/dt = A_{1D}[O^*] \tag{6}$$

where A_{1D} is the sum of the three radiation pathways out of the O(^{1}D) state, each with its own Einstein coefficient (Table 1 in Semeter et al., 1996).

Adding both types of loss (4) and (6) gives

$$L(O^*) = (A_{1D} + Q_T)[O^*] \tag{7}$$

Finally, equating production and loss yields

$$[O^*] = P[O^*]/(A_{1D} + Q_T) \tag{8}$$

This equation allows the concentration of O*(^{1}D) at each altitude to be computed from parameters at that height.

The volume emission rate for the 6300 Å photons at each height is the subset of Eq. (6) for that particular wavelength (given by A_{6300}) as

$$\varepsilon_{6300} = A_{6300}[O^*] (\text{units of photons/cm}^3/\text{s}) \tag{9}$$

Integrating (9) vertically over the full atmosphere gives the column emission rate (or surface brightness viewed from below in photons/cm²/s). With 10^6 photons/cm²/s defined as a Rayleigh (R), the brightness of the SAR arc becomes

$$B_{\text{SAR}} = \frac{A_{6300}}{10^6} \int \left(\frac{P_h(O^*)}{A_{1D} + Q_T} \right) dh$$
(in units of Rayleighs). $\tag{10}$

To perform a simulation of SAR arc brightness, the required parameters are vertical profiles of electron density $N_e(h)$ and electron temperature $T_e(h)$, data that can come from a nearby incoherent scatter radar. The required neutral atmosphere constituents are atomic oxygen O(h) for excitation, plus the molecular gases $O_2(h)$ and $N_2(h)$ for quenching, and these come from MSIS. Some reaction rates require ion temperature $T_i(h)$ and neutral temperature $T_n(h)$, parameters obtained from the ISR and MSIS, respectively. For the heights of interest ($h > 200$ km), the dominant ion is assumed to be O^+, taken to be equal to the electron density.

In addition to the SAR arc, there is the normal 6300 Å airglow that arises from the chemical recombination of the ambient F-layer plasma. Nightglow at 6300 Å arises primarily from the dissociative recombination of O_2^+ with ambient electrons; the O_2^+ must first be derived from the reaction of

O^+ with O_2. The computation of 6300 Å airglow involves the same set of observations and MSIS parameters used for SAR arcs, with the SAR arc production function for O^{1}D in Eq. (3) replaced by its airglow counterpart,

$$P(O^*) = b_r \gamma [O_2][e^-] \tag{11}$$

where b_r is the branching ratio (# of O* produced per dissociative recombination of O_2^+ and e^-), γ is the reaction rate between O^+ and O_2 to form O_2^+, and quantities in brackets are concentrations (Schunk and Nagy, 2000; Solomon and Abreu, 1989).

Volume emission rates can then be computed using (8) and (9) and the total airglow brightness (B_{airglow}) can be obtained in a fashion similar to Eq. (10).

3.2 Millstone Hill observations

While the BU all-sky imager operates every night during two week *lunation periods* (from approximately 3rd quarter to 1st quarter Moon each month), the Millstone Hill ISR is generally constrained to far fewer nights per month for electrical cost and staffing reasons. Thus, most SAR arcs do not have simultaneous ISR data, and thus this event is a rare example of good luck in geophysics. The ISR operated in a local/regional observation mode on 29 October 1991 for a pre-scheduled program of F-layer plasma drift measurements using a multi-point mode (8 positions at 45° elevation angles) which had the radar range gates limited to altitudes below ~500 km. Interspersed with these measurements were zenith profile data on a more rapid cadence in three different modes with correspondingly different range coverage. These data yielded ionospheric information to approximately 800 km maximum altitude, given the radar sensitivity and prevailing electron densities. (For SAR arc science, an ideal scanning program is one limited to the north-south plane with range coverage to 1000 km, and this was used in subsequent Millstone Hill experiments, Foster et al., 1994.) Because of the range constraints on the 45° elevation angle data, temporal continuity is available most completely from the vertical antenna position, and these data are presented in Fig. 7. The ISR data to 800 km was generated using outlier rejection and temporal interpolation of the multiple available zenith observation modes.

The ISR data shown in Fig. 7 begin prior to sunset, well before optical observations are possible. The characteristic signatures of the mid-latitude ionospheric trough appear in these zenith measurements after ~23:00 UT on 28 October 1991: the electron densities (panel a) show a marked transition to lower values, and the electron temperatures change to higher values (panel b). This is the post-sunset time period when the SAR arc was at zenith, but optical observations were not yet possible. The elevated T_e values are no longer present at zenith after ~00:30 UT on 29 October, in excellent agreement with the appearance of the SAR arc south of Millstone Hill in the imaging data (Fig. 4). The occasional
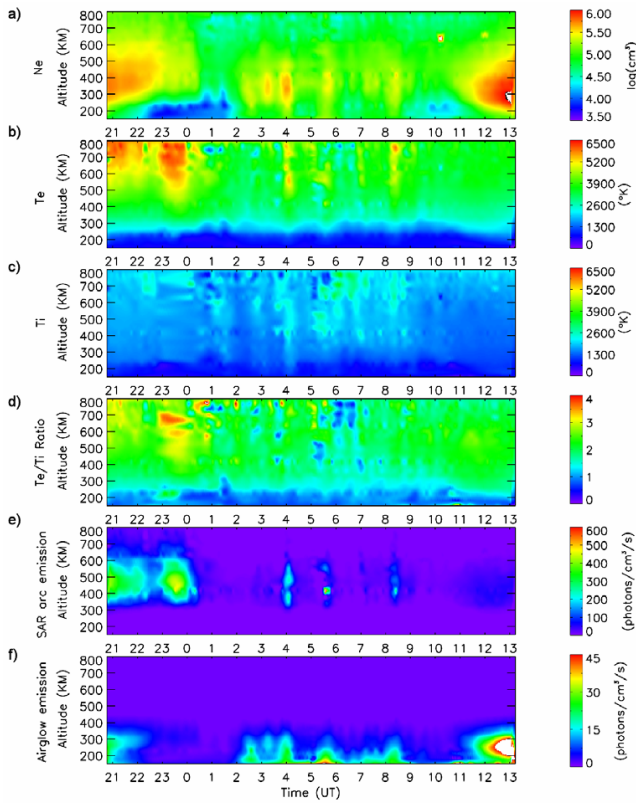
Fig. 7. Time history of ionospheric parameters versus height made at Millstone Hill at times during the night of 28–29 October 1991 when the ISR pointed in the vertical direction: **(a)** electron density, **(b)** electron temperature, **(c)** ion temperature, **(d)** T_e/T_i ratio. Panel **(e)** gives the computed SAR arc volume emission rates, and panel **(f)** the computed airglow volume emission rates. The total modeled SAR arc brightness over this altitude region comes to 10 840 R at 23:32 UT, while the integrated airglow value is 81 R.

Fig. 8. Plasma drift observations converted to electric fields (mV/m) at Millstone Hill on the night of 28–29 October 1991, with 10 m/s corresponding to 1 mv/m. Separate north (y) and east (x) electric fields are indicated.

spikes of ionization during the night (panel a) occurred as the diffuse aurora moved sporadically into the ISR beam (consistent with the images in Fig. 4). To the far right of the figure (after 11:00 UT), all effects are due to sunrise on 29 October 1991.

Using the N_e, T_e and T_i observations in Fig. 7, MSIS compositions, the reaction rates and photo-chemical parameters from Semeter et al. (1996), and the equations from Sect. 2, the 6300 Å brightness values that result from the SAR arc and airglow processes can be computed. The photon volume emission values are shown in panels (e) for the SAR arc and (f) for airglow in Fig. 7; note the different scales used for volume emission values – ones that differ by more than a factor of ten. The SAR arc emission clearly comes from the altitudes and times of high electron temperatures (panel b), at the equatorward edge of the trough (panel a). The integrated brightness at 23:32 UT is 10.8 kR for the SAR arc and 81 R for the 6300 Å airglow. As shown in Fig. 4, when optical observations became possible the SAR arc brightness levels
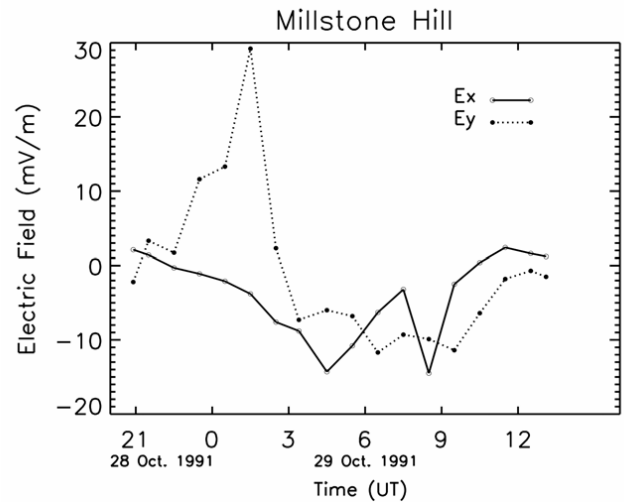
remained comparable (testimony for the use of "stable" in SAR arc terminology).

In addition to the electron density, T_e and T_i measurements, the ISR also made plasma drift measurements on this night. Figure 8 shows electric field values in the Millstone Hill zenith derived from measurements of ion convection. The SAR arc was accompanied by a 30 mV/m excursion in Ey (Northward), corresponding to a westward ion drift of $\sim$300 m/s. These values are similar to those reported by Foster et al. (1994) for a SAR arc that was $\sim$30 times fainter, although their measurements were near the equatorward edge of the arc, while Millstone Hill was closer to the poleward edge of the arc for this event. Nevertheless, the comparable plasma drifts in the sub-auroral region on nights of very different SAR arc brightness levels does not suggest that drift-induced contributions to emission are significant; we discuss this issue quantitatively in Section 5.

3.3 Defense Meteorology Satellite Program (DMSP) data

Figure 9 shows the locations of two DMSP passes near Millstone Hill on the night of the event. Figure 10 presents the values of plasma density, T_e and T_i measured at the $\sim$840 km heights of the satellites versus latitude (and UT). These datasets are crucial for completing the topside profiles missing from the off-zenith ISR observations, and thus special attention was given to their analysis.

The use of these DMSP datasets can, of course, be done only at the two specific times of the satellite passes. As shown in Fig. 2, optical observations had not yet started at the time of the first pass, but the second pass does coincide in time and space with the imaging data. Since the SAR arc
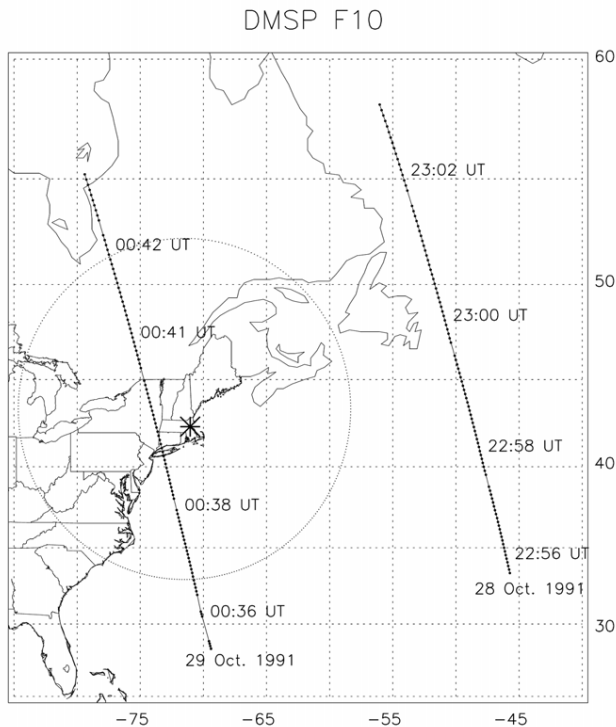
Fig. 9. Map showing the locations of two DMSP over-flights of the Millstone Hill area on the night of 28–29 October 1991.

had already passed by zenith at Millstone Hill, we will use the slant-path observations made by the radar at the 45° elevation angle that intersected the location of the SAR arc in the imager data at the time of the DMSP overflight. The temporal/spatial relationships between the SAR arc image, the radar position and the post-sunset DMSP in situ data are shown in Fig. 11.

3.4 Simulation results

Using the conditions shown in Fig. 11, simultaneous measures of optical emission can be located along the same slanted raypath as the ISR observed plasma conditions. To model that emission, it is necessary first "to complete" the altitude profiles of N_e, T_e and T_i needed for the full optical brightness simulation; such interpolation between the DMSP values and the ISR observations are given by the dashed lines in panels (a) and (b) in Fig. 12. In panel (c) the ion temperature is presented, and compared with the MSIS neutral temperature profile that gives an exospheric temperature value of $T_{exo}=1300$ K for this night. Panels (d), (e) and (f) give the corresponding MSIS neutral densities for O, O_2 and N_2. Panels (g) and (h) give the calculated airglow and SAR arc volume emission profiles, respectively. Finally, in panel (i), the calculation for the SAR arc is re-done using MSIS neutral densities for an exospheric temperature of 1600 K, an upper limit suggested by the Millstone Hill T_i values shown in

panel (c). The results from panels (h) and (i) thus represent modeling uncertainties for the estimated SAR arc brightness values, i.e., 8.6 kR to 23.6 kR. The higher of these values demonstrates the key role of the neutral atmosphere in the SAR arc process. Changing the neutral atmosphere model by 300 K results in enhanced values of atomic and molecular gases in the topside thermosphere. Higher [O] leads to more emission while higher [N_2] and [O_2] lead to more quenching. Clearly, the dominant result is from the enhanced population of O atoms capable of being excited to the ^{1}D state. There are many other sources of modeling uncertainly, e.g., measurement variance in T_e and T_i values extracted from ISR spectral measurements (Foster et al., 1994), but in general these are less uncertain than the neutral compositions on a night of severe geomagnetic activity.

4 Comparisons with previous results

4.1 Previous SAR arc brightnesses

Previous studies of SAR arc brightness values involve an interesting, and certainly controversial, history. In their review of SAR arc observations, Rees and Roble (1975) quote an average brightness of "hundreds of Rayleighs" during the 1970s, with the brightest case being 4 kR for the event on the night of 8–9 March 1970. They contrast this with the report of Roach and Roach (1963) who quoted an *average brightness* of 6 kR during the previous solar cycle. Yet, a careful reading of Roach and Roach suggests that they were discussing only the brightest events (e.g., 29–30 September 1957 at 6 kR, 12–13 November 1960 with 35 kR). Kozyra et al. (1997) raised the issue of calibration accuracy in the 1950s, and thus that the high values (>10 kR) might not be reliable. Yet they point out that emissions in the 6–10 kR range could account for reports of visual low-latitude aurora in Korean historical records of the 16th–17th centuries (Zhang, 1985).

  Hoch (1973) quoted 1 kR as common for SAR arcs during the peak and declining years of the IGY, with "the most intense arc ever detected" as 10 kR in 1958. For the post-IGY solar cycle, Hoch reports 300 R as the typical value with the very brightest at 5 kR, and the faintest at 50 R. Perhaps the most severe challenge to present-day understanding (and calibration methods) comes from the discussion of spectral purity in Roach and Roach (1963) using Barbier's (1960) reported SAR arc with a brightness of 125 kR!

  It seems unwise to question the capabilities of the pioneers of optical aeronomy without additional information. The lack of 2-dimensional low-light-level imaging capabilities in those years also brings up the possibility that the brightest values in the old literature might not refer to pure SAR arcs, but perhaps to features seen upon a background of proton aurora, or even to detached auroral arcs seen during the post-sunset periods at sub-auroral latitudes (Mendillo et al., 1989).
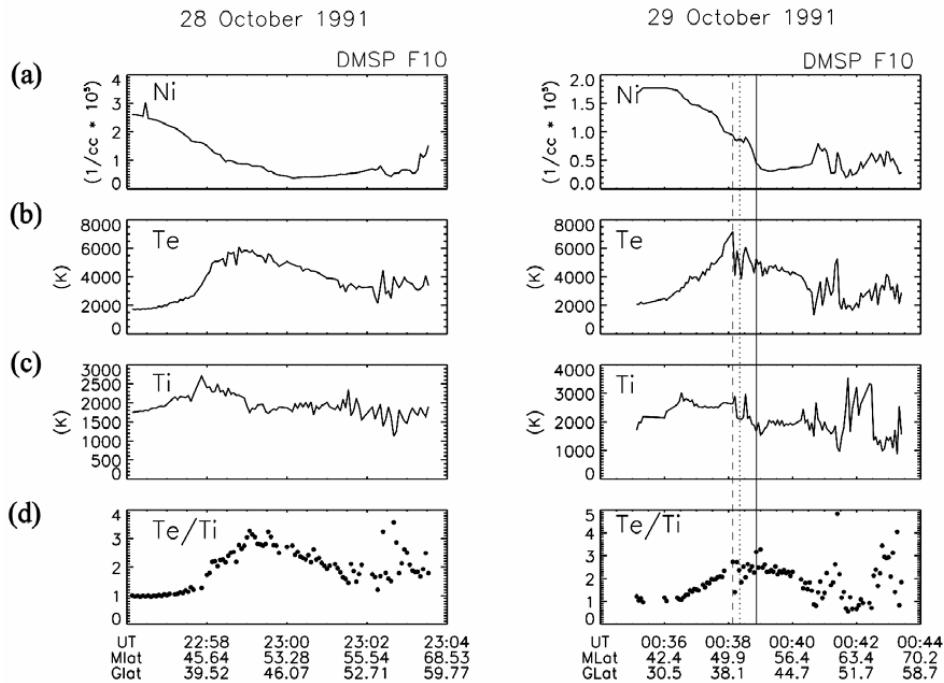
Fig. 10. DMSP plasma parameters for the portions of the over-flight passes shown in Fig. 9. **(a)** plasma density, **(b)** electron temperature, **(c)** ion temperature, **(d)** T_e/T_i ratio, all versus latitude (magnetic and geographic) and time (UT) on 28–29 October 1991. For the pass on the 29th, three times are marked to show the relationship between the DMSP data vs. latitude (dashed line 00:38:08 UT), the ISR off-zenith data (dotted line at 00:38:21 UT), and the 6300 Å image (solid line at 00:38:52 UT). See text and Fig. 11.

The precipitation of ions equatorward of plasma sheet electrons, thereby inducing emissions separate from the diffuse aurora, are a regular feature of large storms (e.g., Mishin and Burke, 2005). Using optical tomography and proton transport code modeling of such an event at Millstone Hill, Lummerzheim et al. (2001) described emission at 6300 Å reaching several kilo-Rayleighs in brightness covering a large portion of the sky for several hours. We will return to the issue of precipitation in Sect. 4.5.

Additional comparisons made locally are possible since observations using a Boston University all-sky camera at Millstone Hill date to the SAR arc recorded on the night of 13 November 1983 (~50 R above background). The SAR arc of 22 March 1990 studied by Foster et al. (1994) was ~100 R above background, as was the event of 5 March 1995 analyzed tomographically by Semeter et al. (1999). As shown in Fig. 1, SAR arcs at Millstone Hill are typically ~500±270 R, a trend that has been consistent from 1983 to 2006. The event of 29 October 1991 at ~10 kR is unquestionably the brightest SAR arc in the BU/Millstone Hill database.

4.2   Previous modeling of SAR arcs

The model results in Fig. 12 are in good agreement with observations. There are several factors that combine to create volume emission rates of ~700 photons/cm^3/s (~100 times
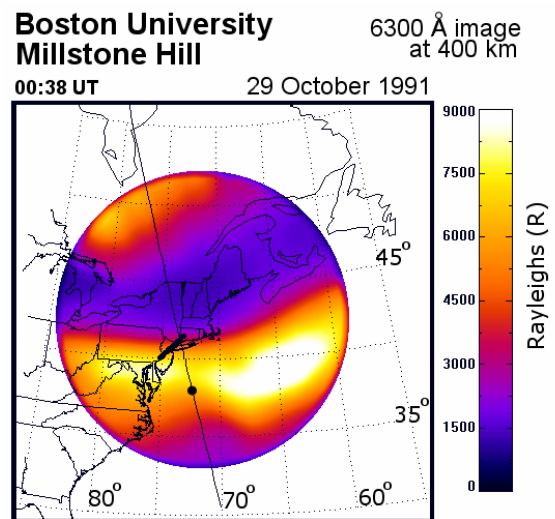

Fig. 11. Spatial/temporal "best match" conditions for the SAR arc in an image: the Millstone Hill ISR measurement intersection (thick black line), and the DMSP point (black dot) for observations of topside plasma parameters for 29 October 1991. The image is at 00:38:52 UT, the ISR data is for 00:38:21 UT and the DMSP data is at 00:38:08 UT.
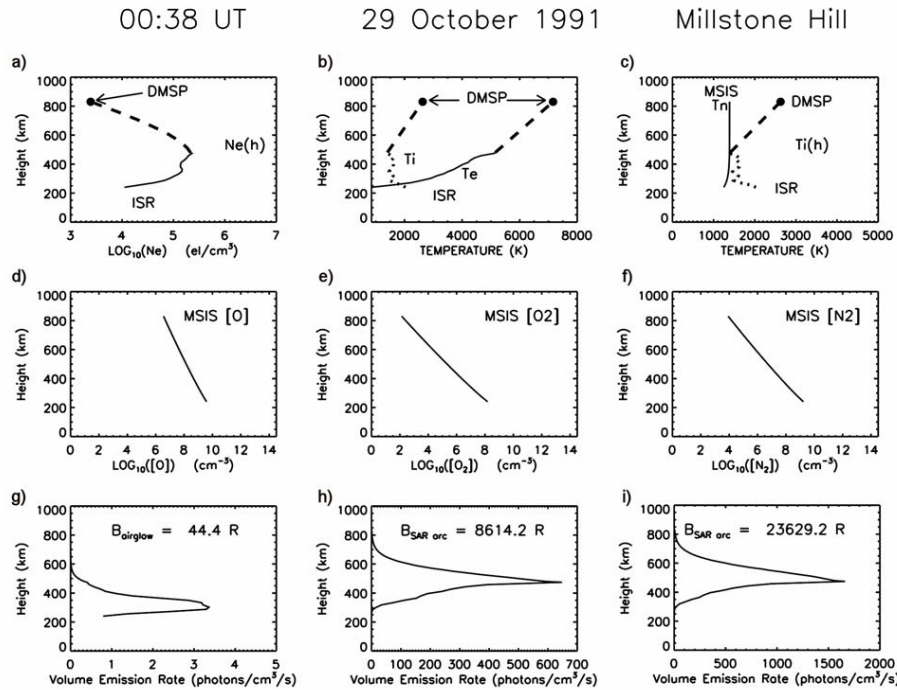
Fig. 12. Summary of input parameters and modeling results for 6300 Å emission on 29 October 1991 for the spatial/temporal conditions shown in Fig. 11. **(a)** $N_e(h)$ from the ISR and DMSP, **(b)** $T_e(h)$ and $T_i(h)$ from the ISR and DMSP, **(c)** Neutral temperature $T_n(h)$ from MSIS giving an exospheric temperature of ~1300 K, shown in comparison to $T_i(h)$, **(d)** O(h) from MSIS, **(e)** O$_2(h)$ from MSIS, and **(f)** $N(h)$ from MSIS. Using the above parameters, simulated volume emission rates for airglow appear in **(g)**, simulated volume emission rates for the SAR arc are shown in **(h)**, and simulated SAR arc emission using MSIS parameters for an exospheric temperature of 1600 K (to assess uncertainties) appear in panel **(i)**.

greater than found for the events in Semeter et al., 1997 and Foster et al., 1994). The main driver for SAR arcs is the local electron temperature, and its thermally-driven emissions increase dramatically once T_e exceeds 3000 K, as occurred on this night (panel (b) in Fig. 10). Typically, a SAR arc occurs within the ionospheric trough where the electron density is $\sim 10^4$ e$^-$/cm^3. This results in a very slow cooling to the ion gas, and hence T_i is generally affected in only minor ways ($\sim$100 s K). For this event, the regions of elevated T_e occurred at latitudes where N_e was considerably higher ($\sim 2 \times 10^5$ e$^-$/cm^3) than found in F-layer trough levels (Fig. 7). The DMSP temperature and density data (Fig. 10) also show that the elevated T_e regions at the time of the image were noticeably equatorward of the trough. This means that there were far more hot electrons to collide with neutral atomic oxygen to excite it to the ^{1}D state, as well as to collide with O$^+$ ions to increase T_i.

In their comprehensive set of SAR arc models, Rees and Roble (1975) presented cases for both "low" electron densities and "high" electron densities for the same set of heat conduction scenarios. The resulting T_e profiles and the 6300 Å SAR arcs they generated resulted in brightness levels of $\sim$3 R to 53 kR. The closest match to this event is their case #7 (NmF2=10^5 e$^-$/cm^3 with heat

flux = 1×10^{11} eV/cm^2/s, giving T_e=8000 K at 1000 km, and a 6300 Å volume emission rate $\sim$400 photons/cm^3/s at 400 km). Those conditions yielded a total brightness of 5.5 kR. Their case #8 (NmF2=2.5×10^5 e$^-$/cm^3/s and heat flux = 2.5×10^{11} eV/cm^2/s, gave T_e=11 000 K at 1000 km, with a peak volume emission rate = 1000 photons/cm^3/s) resulted in a total brightness of 18.5 kR. Thus, the SAR arc of 29 October 1991, as modeled in Fig. 12, is consistent with the average of these types of scenarios calculated 30 years ago.

4.3 Location of the SAR arc

Early insights to SAR arc generation mechanisms associated it spatially and temporally with the ring current-plasmasphere interaction, i.e., a SAR arc occurs "just inside the plasmapause" (Hoch, 1973). Near the footpoint of this boundary lies a region of stagnation in the ionospheric circulation, producing a characteristic depression in F-region plasma density known as the "mid-latitude ionospheric trough" (e.g., Moffett and Quegan, 1983). It appears that the most likely explanation for the anomalous brightness of the 29 October 1991 SAR arc is the relative positions of the trough and the causative heat flux. The implications of

this are discussed in Sect. 5.

In Fig. 13, the location of the 29 October 1991 SAR arc (full width at half brightness), as observed throughout the night, has been mapped (using a fixed emission height of 400 km) along the geomagnetic field lines (using IGRF) to the magnetospheric equatorial plane. This so-called apex mapping then gives the approximate equatorial location of the plasmapause as demonstrated earlier in Pi et al. (2000). Care must be exercised with these mapping results since the very disturbed nature of the magnetic field configuration may have altered field-line trajectories deep within the magnetosphere. Nevertheless, the small extent of the plasmasphere is readily evident and dramatic, with L-shells of ∼2 for many hours. While rare, such contracted states of the plasmasphere are certainly plausible for very large geomagnetic storms (Carpenter and Park, 1973) and their association with SAR arcs has also been well documented (Okano and Kim, 1986). Thus, changes in the configuration of the inner magnetosphere, driven by enhanced solar wind parameters, were at their solar-terrestrial extremes on 28–29 October 1991.

4.4 Other possible sources of emission

The SAR arc under study here appears upon a very bright background (Figs. 4 and 5). Nighttime airglow at 6300 Å in the sub-auroral region is rarely above 100 R, and thus the background values of ∼1000 R cannot be due to the normal chemically-generated redline (as shown in Fig. 12 (panel g), airglow calculated from the measured electron density profiles is ∼80 R). As mentioned in the context of past estimates of brightness values quoted in the literature, an additional contribution from proton precipitation might enhance the overall region of a SAR arc, and particularly so during superstorms. Lummerzheim et al. (2001) analyzed the 6300 Å emission component of a proton aurora observed by the BU imager at Millstone Hill on the night of 11 April 1997. They showed that emissions of a few kR were generated by precipitating protons observed by an overflight of DMSP. In Fig. 14, we give the energetic particles and plasma drift measurements made along the trajectory shown in Fig. 11. A flux of protons was observed equatorward of the region of electron precipitation that drives the diffuse aurora in the northern portion of the image. This is a standard feature for the dusk sector during storms. As in the 11 April 1997 event described by Lummerzheim et al. (2001), a region of very rapid westward ion flow (variously called Sub-Auroral Ion Drift (SAID) or sub-auroral plasma streams (SAPS), see Mishin and Burke, 2005) is again co-located with the region of proton precipitation. The drifts at DMSP altitude are consistent with the 200–300 m/s drifts from the Millstone Hill radar in Fig. 8. This all suggests that the SAR arc occurred within the broad plasmapause boundary layer region (Carpenter and Lemaire, 2004) subjected to ion precipitation. In Fig. 14(top), however, the DMSP 10 keV proton fluxes (shown by Lummerzheim et al. (2001) to cause high visi-
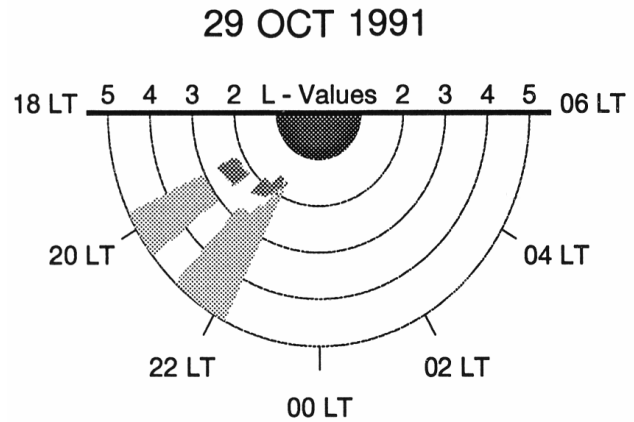

Fig. 13. Locations of the SAR arc (dark shading) and the diffuse aurora (light shading) mapped to the magnetospheric equatorial plane for all available 6300 Å images at Millstone Hill on the night of 29 October 1991. Mapping of the SAR arc was done for an ionospheric emission height of 400 km, while the diffuse aurora were mapped from a height of 200 km.

ble wavelength emission levels) occurred poleward of ∼59° magnetic latitude (about 5° north of Millstone Hill's zenith). In addition to this spatial separation, the ion energy flux is <10^{12} eV/cm^2 s sr for this event, while it was >10^{12} in Lummerzheim et al. (2001).

Proton-induced aurora are readily observed using ground-based instruments (Galand and Chakrabarti, 2006), i.e., from hydrogen emission at visible wavelengths. A careful analysis of the spectrograph data in Fig. 3 revealed that the upper limit to the brightness at the hydrogen (Hα) wavelength of 6563 Å was only 25 R. This is well below the 200–400 R range for Hα reported by Galand et al. (2004) during more moderate geomagnetic conditions. We are left, then, with scattered light from the SAR arc and the nearby aurora as the probable cause of the bright sky. Having two emission regions (aurora to the north, SAR arc to the south), each with ∼10 kR brightness, would certainly lead to a bright sky background, and to sources of scattered light within the optics and detector system. We attribute the high background levels to these effects.

5 Discussion

An intriguing manifestation of magnetosphere-ionosphere (M-I) coupling is the Stable Auroral Red (SAR) arc, first discovered in 1956 by Barbier (1958). During the subsequent half-century, SAR arc characteristics were described and models for their excitation were developed. Attention focused quite naturally on the brightest SAR arcs since they represented case studies of strong M-I coupling easily observed by photometers and readily addressed by modeling. Virtually all of those achievements occurred prior to the
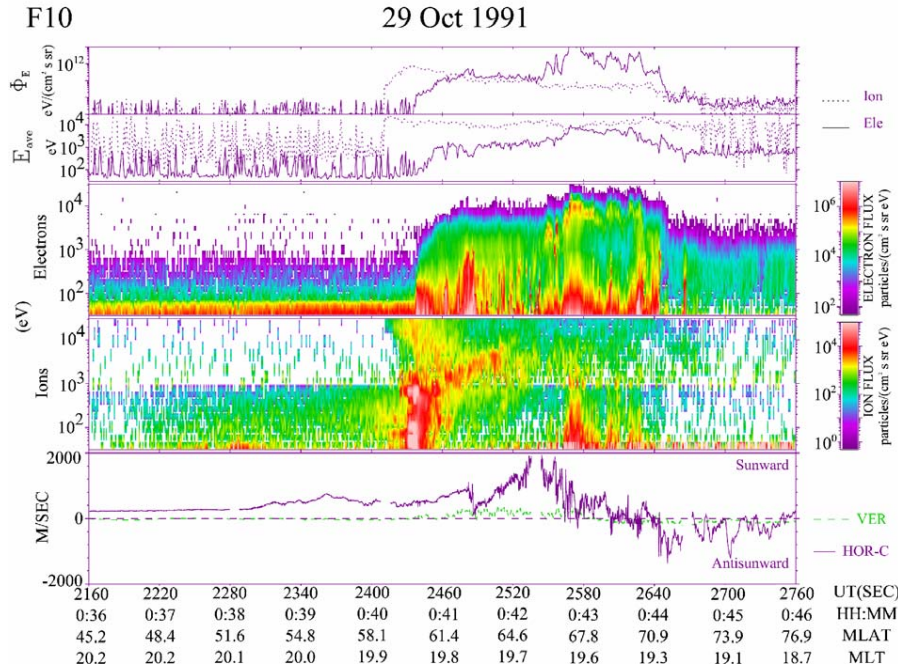
Fig. 14. DMSP data for energetic electrons and ions and bulk plasma drift along the trajectory shown in Fig. 11 at the time of the SAR arc.

widespread use of groundbased low-light-level imaging systems that can document the 2-dimentional patterns of SAR arc brightness. Moreover, those studied occurred prior to the use of incoherent scatter radar (ISR) diagnostics to specify the ionospheric state parameters within a SAR arc, and prior to the use of in-situ satellite data to describe the signatures of particles and fields of magnetospheric origin upon the topside ionosphere. When such observations became available at Millstone Hill (Mendillo et al., 1987; Foster et al., 1994; Semeter et al., 1999), the SAR arc events observed were at the extremely faint end of brightness values (~50 R to ~few 100 R). These events offered challenges, as pointed out by Kozyra et al. (1997), since the observed ionospheric electron temperatures appeared to be insufficient to account for such low brightness SAR arcs. This led to re-assessments of heating mechanisms (e.g., by electromagnetic ion cyclotron (EMIC) waves by Konikov and Pavlov, 1991), and to the efficiency of trough formation (e.g., by N_2-vibrationally enhanced loss chemistry by Pavlov, 1996). Sazykin et al. (2002) examined non-thermal pathways to excite $O(^1D)$ via ion-neutral collisions within polarization jet events observed within SAR arc regions. Surprisingly, no cases of very bright SAR arcs were subjected to detailed analysis and modeling to validate the thermal excitation mechanism in its peak occurrence mode. The superstorm event of 29 October 1991 now offers such a case study.

We have conducted a thorough re-calibration of two imaging datasets from the Boston University CEDAR Optical Facility at the Millstone Hill/Haystack Observatory on the night of 29 October 1991. This resulted in a peak value of above-atmosphere brightness of 13 500 R±20%. This is by far the brightest SAR arc value in two solar cycles of observations at Millstone Hill, where long term averages yield observed brightnesses of 500 R±270 R (with the same 20% uncertainty). Using a combination of Millstone Hill ISR profiles of ionospheric densities and temperatures, DMSP topside data, the MSIS atmospheric model and the Rees and Robel (1975) theoretical framework, values of brightness in the range 8.6 kR to 23.7 kR were calculated. Since the higher model value came from estimates of maximum possible MSIS uncertainty, the match to an extinction corrected brightness of 13.5 kR is considered satisfactory.

It has been suggested (see Sazykin et al., 2002) that electric fields associated with sub-auroral ion drifts (SAIDs) may provide a significant additional heat source for the ambient electrons within SAR arcs, thus contributing to the SAR arc brightness. To evaluate this possibility for the event at issue, consider the equilibrium electron temperature perturbation ΔT_e for a given electric field magnitude E. Assuming $T_i=T_e$, this may be expressed as (Brekke, 1997)

$$\Delta T_e = \frac{m_i}{3kB^2\left[\left(\upsilon_{in}/\Omega_i\right)^2 + 1\right]}E^2 \qquad (12)$$

where m_i is the ion mass, k is Boltzman's constant, $\upsilon_{\rm in}$ is the ion-neutral collision frequency, and Ω_i is the ion gyrofrequency. Using the measured electric field of 30 mV/m (Fig. 8) and a typical SAR arc emission altitude of 350 km (Semeter et al., 1999), we find that ΔT_e=400 K. To become

a significant source of O(^{1}D), the electron gas must have a significant density in the high energy tail above 1.96 eV (the excitation potential). This requires $\Delta T_e > 3000$ K (Rees and Roble, 1975), or $E > 85$ mV/m. The measured electric fields would have to be underestimated by a factor of 3 for this mechanism to have contributed to this event. Even given the inherent uncertainties in estimating E using a monostatic ISR, such a severe underestimation is unlikely. Thus, it is noteworthy that for the brightest SAR arc ever observed over Millstone Hill we find no evidence for a significant electric field contribution to the emission brightness.

The observed electron temperatures ranged from ∼4000 K at 400 km to ∼9000 K at the DMSP height of 840 km. The downward heat conduction from ring current sources that creates these high temperatures to drive the SAR arc emission is estimated to be in the range ∼2×10^{11} eV/cm^2/s, taken from the library of modeling results in Rees and Roble (1975) that best match the conditions on the night of 29 October 1991. The effectiveness of this flux is not so much from the temperatures achieved (though they are certainly elevated), but from the fact that the electron densities being heated are so high. At Millstone Hill, typical values of the peak electron density in the nighttime sub-auroral F-layer's ("main") trough are ∼2–3×10^4 e$^-$/cm^3 when SAR arcs are seen (e.g., Mendillo et al., 1987; Foster et al., 1994). As shown in Figs. 7 and 12, on the night of 29 October 1991, the peak electron density was an order of magnitude higher. Thus, with more than 10^5 e$^-$/cm^3 at 450 km heated to $T_e = 5000$ K, frequent collisions with ∼10^8 oxygen atoms/cm^3 produced large volume emission rates, as shown in panel (h) of Fig. 12.

The DMSP data for this night (panels (a) and (b) in Fig. 10) show that the elevated T_e values, and thus the SAR arc's location, are not at the trough's minimum, but along its equatorward edge (typical of the plasmapause boundary). The extreme brightness of this SAR arc thus appears to be a consequence of an unusual offset between the ionospheric trough (i.e., the stagnation region in the sub-auroral magnetospheric convection) and downward heat flux (produced by ring-current decay). Examination of Fig. 2 suggests that the effect may, in fact, be temporal. Statistically, SAR arcs are most likely to occur during the recovery phase of a magnetic storm (Kozyra et al., 1997), yet this one – the brightest ever observed at Millstone Hill – occurred early in the main phase of the storm, as clearly indicated by Dst.

A review of solar wind data suggests one possible explanation. At 00:00 UT on 29 October 1991, strong (∼-10 nT) southward IMF arrived at the IMP-8 satellite located just 20 R$_E$ or ∼2.7 minutes travel time upstream of the Earth's magnetopause. This was very close to the time of the SAR arc intensification. It is possible that the abrupt onset of strong magnetospheric convection produced by the arrival of the southward IMF brought a front of ions (referred to as a "nose event" (Smith and Hoffman, 1974; Kozyra et al., 1993)) into the inner magnetosphere. Nose events consist of ions (mostly H$^+$) with peak flux in the energy range of 10–30 keV but ex-

tending down to keV energies. H$^+$ ions in this energy range transfer their energy effectively to the thermal electrons in the plasmasphere, which then support strong heat fluxes along magnetic field lines into the ionospheric plasma. Kozyra et al. (1993) calculated the column heating due to Coulomb collisions between energetic ions and thermal plasmaspheric electrons for one such nose event on 19 September 1984 during the main phase of a magnetic storm and found H$^+$ at the low end of the ring current energy range (10's of keV) to be responsible for the majority of the heating.

In a study of some 400 nose events, Ganushkina et al (2000) found deepest penetration (∼0.4–0.6 R$_E$) of low energy ring current ions into the plasmasphere in the midnight and dusk local time sectors. For the current study, DMSP observations were taken near 20.5 MLT. This may be why the T_e peak is initially equatorward of the minimum densities in the ionospheric trough by $\Delta L \sim 0.3$ R$_E$. An examination of subsequent DMSP measurements showed that the T_e peak became coincident with the trough minimum later in the storm cycle (near ∼04:00 UT). This adjustment to the more common SAR arc configuration could be associated with the arrival of the bulk of the ring current in the outer plasmasphere, which moved the peak T_e closer to the plasmapause. While somewhat speculative, this discussion suggests a new role of SAR arc observations in studies of time-dependent solar wind-magnetosphere coupling.

6 Conclusions

The case study presented here constitutes a test of the theory of SAR arc formation under extreme conditions of solar wind-magnetosphere coupling. Although the peak brightness was extreme (a factor of ∼20 above average), it was ultimately found to be consistent with in-situ and ground-based measurements of electron temperature and electron density. We thus conclude that the aeronomy of SAR arc production is well understood over the full range of occurrence of this phenomenon. (Kozyra et al., 1997; Lobzin and Pavlov, 1999) The extremely high brightness levels were due to the heating of electron densities not in the trough (as occurs with most SAR arcs), but the higher N_e values equatorward of the trough, possibly due to nose-type heating scenarios in the dusk sector.

This agreement between theory and observation suggests a possibly expanded role for mid-latitude monochromatic imaging in event-driven studies of geomagnetic storms. The 29 October 1991 event suggests that the brightness of SAR arcs is regulated by the relative location (in both space and time) of enhanced heat flux and the mid-latitude ionospheric trough. Further analysis of conjugate ground-based and space-borne data sets may establish SAR arc brightness as a time-dependent measure of the relative location between the ring-current-plasmasphere boundary and the convection-related mid-latitude trough, thereby establishing calibrated
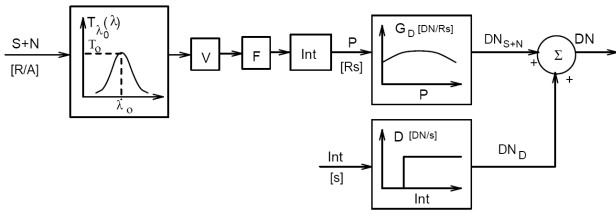
Fig. A1. Block diagram of linear system representing the relationship between incoming photon flux ($S+N$) and corresponding data number.

SAR arc measurements as a critical space weather diagnostic.

Appendix A

Photometric calibration of all-sky spectral imager

Quantitative studies of the aurora and airglow using spectral imaging systems require careful calibration of image data numbers [DN] to brightness in Rayleighs (R) (Hunten et al., 1956). This appendix describes the calibration technique applied to the Boston University all-sky imaging system used in this study. The technique is generally applicable to any intensified imaging system using narrow-band filters.

At a single pixel, a digital imaging system can be modeled as a linear system acting on a photon flux. A block diagram is shown in Fig. A1. Treating the input signal as a spectral intensity (R/Å versus wavelength λ we have the following definitions (italics indicate wavelength dependent variables):

S	Desired input signal [R/Å]
N	Unwanted background continuum [R/Å]
T_λ	Transmission curve for narrow-band interference filter with center wavelength λ_0
V	Vignetting function (function of radial distance from the optical axis)
F	Flat field adjustment (pixel-to-pixel variation in sensitivity)
Int	Integration (exposure) time of image [s]
G_D	Detector gain [DN/R-s] (constant for an ideal detector)
D	Dark count rate [DN/s]. Includes contributions from image intensifier and CCD detector
DN	Resulting data number

The block diagram leads to the following equation for the data number at a given pixel through filter characterized by λ_0

$$DN_{\lambda 0} = FV \text{Int} G_D \int_0^\infty (S+N) T_{\lambda 0} d\lambda + \text{Int} D \tag{A1}$$

where S, N, and T_λ are understood to be functions of wavelength. All of the spectral energy under T_λ is concentrated

onto a single pixel, which gives rise to the integration over wavelength. Each DN results from a summation of a desired signal S and unwanted background N which must be removed.

Our signal is assumed to be a single spectral feature that may be isolated using a filter of sufficiently narrow bandwidth. Within the pass-band of the filter, N is assumed to be constant such that $\int_0^\infty NT_{\lambda 0} d\lambda = NA_{\lambda 0}$ where A_λ is the integrated area (in Å) under the filter transmission curve. Furthermore, we assume that the energy of S is concentrated at λ_0 such that $\int_0^\infty ST_{\lambda 0} d\lambda = \int_0^\infty S\delta(\lambda_0) T_{\lambda 0} d\lambda = ST_0$, where δ is the Dirac delta function and T_0 is the filter transmission at λ_0 Eq. (A1) may then be written

$$DN_{on} = FV \text{Int}_{on} G_D (ST_0 + NA_{on}) + \text{Int}_{on} D \tag{A2}$$

where the subscript "on" indicates that these variables refer to the "on-band" filter. Note that the italics have been removed from S and N, indicating that they now refer to integrated intensities, or brightnesses, in Rayleighs. Solving for S gives

$$S = \frac{1}{T_0} \left[\frac{DN_{on} - \text{Int}_{on} D}{FVG_D \text{Int}_{on}} - NA_{on} \right] \tag{A3}$$

The unknown quantities are N, G_D, and D. N is determined using an "off-band" filter at a wavelength near the desired signal, but where no emission lines are present. The off-band filter used for the OI 6300 Å images in this is centered at 6444 Å. Measurements using the off-band filter may be used to determine N as follows. Following the previous development, but with $S=0$ and using an off-band filter, N is given by

$$N = \frac{DN_{off} - \text{Int}_{off} D}{FVG_D \text{Int}_{off} A_{off}} \tag{A4}$$

The detector gain G_D is estimated by showing the imaging system (with on-band filter) a Carbon-14 light source of known intensity S_{C14}. Over the pass band of a typical interference filter S_{C14} is very nearly constant, resulting in a similar expression to Eq. (A4)

$$S_{C14} = \frac{DN_{C14} - \text{Int}_{on} D}{FVG_D \text{Int}_{on} A_{on}} \tag{A5}$$

Solving for the detector gain we have

$$G_D = \frac{1}{FVA_{on}} \left[\frac{DN_{C14} - \text{Int}_{on} D}{S_{C14} \text{Int}_{on}} \right] = \frac{\text{Cal}}{FVA_{on}} \tag{A6}$$

The equation is written this way to indicated that the C-14 source may be used to derive a single "calibration image," Cal$=G_D FV A_{on}$ [DN-Å/R-s], that includes gain, vignetting, and flat-field information. This image is difficult to obtain for a wide-field lens since standard calibration sources will not fill the field of view.

In an ideal detector G_D is constant and is thus determined through a single measurement of DN_{C14} for a given Int$_{on}$.

In practice, measurements of G_D for a variety of integration times show a slight variation for low and high data numbers caused by nonlinearities in the image intensifier gain and/or gamma corrections in the camera. For this reason, an empirically determined function for G_D should be fitted from multiple measurements.

The dark count rate D is determined by closing off the aperture to all light and measuring DN_D. For our Pullnix CCD camera, D was found to be 0 for integration times less than a few seconds, increasing linearly above this threshold. As with G_D, an empirical function can be constructed using measurements over a range of integration times. In practice, DN_D is often measured for only the integration times used in a particular experiment.

Combining Equations (A2–A6), we may express the calibrated brightness of the desired signal in terms of measured quantities

$$S = \frac{A_{\mathrm{on}}}{T_0 \mathrm{Cal}} \left[\frac{(DN_{\mathrm{on}} - \mathrm{Int}_{\mathrm{on}} D)}{\mathrm{Int}_{\mathrm{on}}} - \frac{(DN_{\mathrm{off}} - \mathrm{Int}_{\mathrm{off}} D)}{\mathrm{Int}_{\mathrm{off}}} \cdot \frac{A_{\mathrm{on}}}{A_{\mathrm{off}}} \right] \text{(A7)}$$

Equation (A7) is a practical calibration equation. Note that the Cal image must be recorded with sufficiently long averaging to produce a result independent of statistical noise. Systematic uncertainties in absolute calibration are introduced primarily through G_D and D. Uncertainties in pixel-to-pixel sensitivity arise from uncertainties in F and V.

References

Allen, C. W.: Astrophysical Quantities, Athlone, London, 1973.

Barbier, D.: L'activite aurorale aux bass latitudes, Ann. Geophys., 14, 334–355, 1958,
http://www.ann-geophys.net/14/334/1958/.

Barbier, D.: L'arc auroral stable, Ann. Geophys., 16, 544–549, 1960,
http://www.ann-geophys.net/16/544/1960/.

Baumgardner, J., Flynn, B., and Mendillo, M.: Monochromatic imaging instrumentation for applications in aeronomy of the earth and planets, Opt. Eng., 32, 3028–3032, 1993.

Bell, J. T., Gussenhoven, M. S., and Mullen, E. G.: Super Storms, J. Geophys. Res., 102, 14 189–14 198, 1997.

Brekke, A., Physics of the Polar Upper Atmosphere, Wiley-Praxis Series in Atmospheric Physics, John Wiley & Sons Inc, 1997.

Carpenter, D. L. and Lemaire, J.: The plasmasphere boundary layer, Ann. Geophys., 22, 4291–4298, 2004,
http://www.ann-geophys.net/22/4291/2004/.

Carpenter, D. L. and Park, C. G.: On what ionospheric workers should know about the Plasmapause-plasmasphere, Rev. Geophys. Space Phys., 11, 133–154, 1973.

Cole, K. D.: Stable auroral red arc, sinks for energy of Dst main phase, J. Geophys. Res., 70, 1689–1706, 1965.

Evans, J.V. and Loewenthal, M., Ionospheric backscatter observations. Planet. Space Sci. 12, 913-920. 1964.

Foster, J. C., Buonsanto, M. J., Mendillo, M., Nottingham, D., Rich, R. J., and Denig, W.: Coordinated stable auroral red arc observations: Relationship to plasma convection, J. Geophys. Res., 99, 11 429–11 439, 1994.

Galand, M., Baumgardner, J., Pallamraju, D., Chakrabarti, S., Løvhuag, U. P., Lummerzheim, D., Lanchester, B. S., and Rees, M. H.: Spectral imaging of proton aurora and twilight at Tromsø, Norway., J. Geophys. Res., 109, A07305, doi:10.1029/2003JA10033, 2004.

Galand, M. and Chakrabarti, S.: Proton aurora observed from the ground, J. Atmos. Sol.-Terr. Phy., 68, 1488–1501, 2006.

Ganushkina, N. Y., Pulkkinen, T. I., Sergeev, V. A., Kubyshkina, M. V., Baker, D. N., Turner, N. E., Grande, M., Kellett, B., Fennell, J., Roeder, J., Sauvaud, J.-A., and Fritz, T. A.: Entry of plasma sheet particles into the inner magnetosphere as observed by Polar/CAMMICE, J. Geophys. Res., 105, 25 205–25 219, 2000.

Greenspan, M. E., Anderson, P. B., and Pelagatti, J. M.: Characteristics of the thermal plasma monitors (SSIES) for the Defense Meteorological Satellite Program (DMSP) spacecraft S8 through F10, Tech. Rep. AFGL-TR-86-0227, Air Force Geophys. Lab., Hanscom AFB, MA, 1, 1986.

Hoch, R. J.: Stable auroral red arcs, Rev. Geophys. Space Phys., 11, 935–949, 1973.

Hunten, D. M., Roach, F. E., and Chamberlain, J. W.: A photometric unit for the airglow and aurora, J. Atmos. Terr. Phys., 8, 345–346, 1956.

Konikov, Yu. U. and Pavlov, A. V., On airglow of 630 nm wavelength in the SAR-arcs Region, Ann. Geophys., 9, 540–545, 1991,
http://www.ann-geophys.net/9/540/1991/.

Kozyra, J. U., Chandler, M. O., Hamilton, D. C., Peterson, W. K., Klumpar, D. M., D. Slater, W., Buonsanto, M. J., and Carlson, H. C.: The role of ring current nose events in producing stable auroral red arc intensifications during the main phase: Observations during the September 19–24 1984, Equinox transition study, J. Geophys. Res., 98(A6), 9267–9284, 1993.

Kozyra, J. U., Nagy, A. F., and Slater, D. W.: High-altitude energy source(s) for stable auroral red arcs, Rev. Geophys., 35, 155–190, 1997.

Lobzin, V. V. and Pavlov, A. V.: Correlations between SAR arc intensity and solar and geomagnetic activity, Ann. Geophys., 17, 770–781, 1999,
http://www.ann-geophys.net/17/770/1999/.

Lummerzheim, D., Galand, M., Semeter, J., Mendillo, M. J., Rees, M. H., and Rich, F. J.: Emission of OI(630 nm) in proton aurora,

J. Geophys. Res., 106, 141–148, 2001.

Mac-Mahon, R. M. and Gonzalez, W. D.: Energetics during the main phase of geomagnetic superstorms, J. Geophys. Res., 102, 14 199–14 207, 1997.

Mendillo, M. and Baumgardner, J.: Ground-based imaging of detached arcs, ripples in the diffuse aurora, and patches of 6300 Å emission, J. Geophys. Res., 94, 5367–5381, 1989.

Mendillo, M., Baumgardner, J., Aarons, J., Foster, J., and Klobuchar, J.: Coordinated optical and radio studies of ionospheric disturbances: Initial results from Millstone Hill, Ann. Geophys., 5A(6), 543–550, 1987.

Mishin, E. V. and Burke, W. J.: Stormtime coupling of the ring current, plasmasphere, and topside ionosphere: Electromagnetic and plasma disturbances, J. Geophys. Res., 110, A07209, doi:10.1029/2005JA011021, 2005.

Mishin, E. V., Burke, W. J., and Viggiano, A. A.: Stormtime subauroral density troughs: Ion-molecule kinetics effects, J. Geophys. Res., 109, A10301, doi:10.1029/2004JA010438, 2004.

Moffett, R. J. and Quegan, S.: The mid-latitude trough in electron concentration of the ionospheric F layer: A review of observations and modeling, J. Atmos. Terr. Phys., 45, 315–343, 1983.

Noxon, J. F. and Evans, J. V.: Simultaneous optical and incoherent scatter observations of two low-latitude auroras, Planet. Space Sci., 24, 425–442, 1976.

Okano, S. and Kim, J. S.: SAR arc and concurrent auroral electrojet activity, Planet. Space Sci., 34, 363–369, 1986.

Pavlov, A. V.: Mechanisms of the electron density depletion in the SAR arc region, Ann. Geophys., 14, 211–221, 1996, http://www.ann-geophys.net/14/211/1996/.

Pi, X., Mendillo, M., Hughes, W. J., Buonsanto, M. J., Sipler, D. P., Kelly, J., Zhou, Q., Lu, G., and Hughes, T. J.: Dynamical effects of geomagnetic storms and substorms in the middle-latitude ionosphere: An observational campaign, J. Geophys. Res., 105, 7403–7417, 2000.

Rees, M. H. and Roble, R. G.: Observations and theory of the formation of stable auroral red arcs, Rev. Geophys. Space Phys., 13, 201–242, 1975.

Rees, M. H., Walker, J. C. G., and Dalgarno, A.: Auroral excitation of the forbidden lines of atomic oxygen, Planet. Space Sci., 15, 1097–1110, 1967.

Rich, F. J. and Hairston, M.: Large-scale convection patterns observed by DMSP, J. Geophys. Res., 99, 3827–3844, 1994.

Roach, F. E. and Roach, J. R.: Stable 6300 Å auroral arcs in mid-latitudes, Planet. Space Sci., 11, 523–545, 1963.

Sazykin, S., Feyer, B. G., Galperin, Y. I., Zinin, L. V., Grigoriev, S. A., and Mendillo, M.: Polarization jet events and excitation of weak SAR arcs, Geophys. Res. Lett., 29, 12, doi:10.1029/2001GL014388, 2002.

Schunk, R. W. and Nagy, A. F.: Ionospheres: Physics, Plasma Physics and Chemistry, Camb. Univ. Press, Cambridge (UK), 2000.

Semeter, J. L.: Groundbased Tomography of Atmospheric Optical Emissions, Ph. D. dissertation, College of Engineering, Boston University, 1997.

Semeter, J., Mendillo, M., and Baumgardner, J.: Multispectral tomographic imaging of the midlatitude aurora, J. Geophys. Res., 104, 24 565–24 585, 1999.

Semeter, J., Mendillo, M., Baumgardner, J., Holt, J., Hunton, D. E., and Eccles, V.: A study oxygen 6300 Å airglow production through chemical modification of the nighttime ionosphere, J. Geophys. Res., 101, 19 683–19 699, 1996.

Smith, P. H. and Hoffman, R. A.: Direct observation in the dusk hours of the characteristics of the storm time ring current particles during the beginning of magnetic storms, J. Geophys. Res., 79, 966–967, 1974.

Solomon, S. C. and Abreu, V. J.: The 630 nm dayglow, J. Geophys. Res., 94, 6817–6824, 1989.

Zhang, Z.: Korean auroral records of the period AD 1507–1747 and the SAR arcs, J. Brit. Astron. Assoc., 95, 205, 1985.